

# Photoproduction of jets at HERA in next-to-leading order QCD

B.W. Harris and J.F. Owens  
*Physics Department*  
*Florida State University*  
*Tallahassee, Florida 32306-3016, USA*  
(April 1997)

## Abstract

A new next-to-leading order Monte Carlo program for the calculation of jet cross sections in photoproduction is described. The contributions from both resolved and direct components are included to  $\mathcal{O}(\alpha_s^2)$ . Properties of the predictions for various inclusive jet and dijet observables are discussed and comparisons with HERA data are presented.

PACS number(s): 12.38.Bx,13.60.Hb,14.70.Bh

arXiv:hep-ph/9704324v2 16 Jun 1997

## I. INTRODUCTION

Electromagnetic interactions have long been used to study both hadronic structure and strong interaction dynamics. Examples include deep inelastic lepton-nucleon scattering, hadronic production of lepton pairs, the production of photons with large transverse momenta, and various photoproduction processes involving the scattering of real or very low mass virtual photons from hadrons. In particular, the photoproduction of jets with large transverse momenta is calculable in QCD and offers additional complementary information to that obtained from the study of the hadroproduction of jets [1]. In the photoproduction case there are contributions where the photon's energy contributes entirely to the hard-scattering subprocess; these are often referred to collectively as the direct component. In addition, a real photon can interact via its hadronic substructure. These contributions comprise the resolved component, a review of which is contained in Ref. [2]. Therefore, the photoproduction of jets allows one to investigate new production mechanisms, probe the hadronic substructure of the photon, and study the conventional hadronic jet production mechanisms which these processes have in common with the hadroproduction case.

Two basic approaches are commonly employed for generating predictions for hard-scattering processes. On the one hand, it is possible to perform calculations for a specific observable in which the integrals over the subprocess variables are done analytically, leaving only the convolutions with the parton distributions to be done numerically. On the other hand, if the subprocess integrations and the parton distribution convolutions are done using Monte Carlo techniques, it is possible to generate predictions for a variety of different observables simultaneously. This latter approach is sometimes referred to as a fully differential Monte Carlo calculation. Several groups have performed next-to-leading-order calculations of jet photoproduction in varying degrees of generality using one or the other of these two approaches. In [3], [4], and [5] subprocesses which involved the photon were kept up to  $\mathcal{O}(\alpha\alpha_s^2)$ . Thus, the direct component was calculated to next-to-leading-logarithm accuracy while the resolved component was calculated in the leading-logarithm approximation. The resolved component was calculated to next-to-leading-logarithm accuracy in [6], [7], [8], and [9] for single inclusive production. For a review see [10]. Recently, both direct and resolved contributions calculated to next-to-leading-logarithm accuracy have begun to appear [11], [12], [13] in a fully differential form.

The purpose of this work is to present a discussion of a calculation which is based on the phase space slicing method using two cutoffs [14]. Both the direct and resolved components are included to next-to-leading-logarithm accuracy. The result is fully differential and implemented in a Monte Carlo style program which allows the simultaneous histogramming of many distributions incorporating experimental cuts. It represents an improvement of earlier results which included the direct component only at NLO [3] and an elaboration of the very brief results for both components already presented [11]. Details of the calculational method are presented as well as comparisons with recent data. Some comments on various unsettled issues that arise when comparing with dijet cross sections are also given.

The remainder of the paper is as follows. The phase space slicing method is reviewed in Sec. II. Numerical results are compared with H1 and ZEUS data and related physics issues are discussed in Sec. III, while the conclusions are given in Sec. IV.

## II. METHOD

In this section we describe the calculation of QCD corrections to two-jet production in electron-proton scattering using the phase space slicing method. Before discussing the QCD corrections, it is necessary to recount the connection between electron-proton and photon-proton scattering. For small photon virtualities  $Q^2$  the two are related using the Weizsäcker-Williams approximation [15] wherein one assumes that the incoming electron beam is equivalent to a broad-band photon beam. The cross section for electron-proton scattering is then given as a convolution of the photon distribution in an electron and the photon-proton cross section

$$d\sigma(ep \rightarrow eX) = \int_{y_{\min}}^{y_{\max}} dy F_{\gamma/e}(y) d\sigma(\gamma p \rightarrow X). \quad (2.1)$$

The integration limits and the maximum photon virtuality  $Q_{\max}^2$  are determined from the (anti) tagging conditions of the experiment. The energy of the photon is related to the energy of the incident electron by  $E_\gamma = yE_e$ . We used the improved photon distribution in an electron [16] given by the formula

$$F_{\gamma/e}(y) = \frac{\alpha_{\text{em}}}{2\pi} \left\{ \frac{1 + (1-y)^2}{y} \ln \frac{Q_{\max}^2(1-y)}{m_e^2 y^2} + 2m_e^2 y \left[ \frac{1}{Q_{\max}^2} - \frac{(1-y)}{m_e^2 y^2} \right] \right\} \quad (2.2)$$

where  $m_e$  is the electron mass and  $\alpha_{\text{em}}$  is the electromagnetic coupling. Within this approximation, QCD corrections to electron-proton scattering correspond to QCD corrections to photon-proton scattering to which we now turn.

In this version of the phase space slicing method [14] two small cutoffs  $\delta_s$  and  $\delta_c$  are used to delineate regions of phase space where soft and collinear singularities occur. Let the four vectors of the three-body subprocesses be labeled  $p_1 + p_2 \rightarrow p_3 + p_4 + p_5$ , and define the Mandelstam invariants  $s_{ij} = (p_i + p_j)^2$  and  $t_{ij} = (p_i - p_j)^2$ . Consider, for example, the  $\gamma(p_1)g(p_2) \rightarrow q(p_3)\bar{q}(p_4)g(p_5)$  subprocess whose matrix element becomes singular as the energy  $E_5$  of the final state gluon becomes soft. Define the soft region  $S$  by  $0 < E_5 < \delta_s \sqrt{s_{12}}/2$  and the complementary hard region  $H$  by  $\delta_s \sqrt{s_{12}}/2 < E_5 < \sqrt{s_{12}}/2$ , both in the  $p_1 + p_2$  rest frame. The two-to-three body contribution to the cross section is then decomposed as

$$\begin{aligned} \sigma &= \frac{1}{2s_{12}} \int |M|^2 d\Gamma_3 \\ &= \frac{1}{2s_{12}} \int_S |M|^2 d\Gamma_3 + \frac{1}{2s_{12}} \int_H |M|^2 d\Gamma_3 \end{aligned} \quad (2.3)$$

where  $|M|^2$  is the three-body squared matrix element and  $d\Gamma_3$  is the three-body phase space. Within  $S$  one sets  $p_5 = 0$  *everywhere* except in the denominators of the matrix elements and then analytically integrates over the unobserved degrees of freedom in  $n$  space-time dimensions. The result, proportional to the leading order cross section, contains double and single poles in  $n - 4$ , and double and single logarithms in the soft cutoff  $\delta_s$ . Terms of order  $\delta_s$  are neglected. Next, the collinear regions of phase space are defined to be those where

any invariant ( $s_{ij}$  or  $t_{ij}$ ) becomes smaller in magnitude than  $\delta_c s_{12}$ . The hard region is then decomposed into collinear  $C$ , and non-collinear  $\overline{C}$ , regions as follows:

$$\frac{1}{2s_{12}} \int_H |M|^2 d\Gamma_3 = \frac{1}{2s_{12}} \int_{HC} |M|^2 d\Gamma_3 + \frac{1}{2s_{12}} \int_{H\overline{C}} |M|^2 d\Gamma_3. \quad (2.4)$$

Within  $HC$  one retains only the leading pole of the vanishing invariant in the squared matrix elements. Exact collinear kinematics are used to define the integration domain of  $HC$ , which is valid so long as  $\delta_c \ll \delta_s$ . The integrations over the unobserved degrees of freedom are then performed analytically in  $n$  space-time dimensions giving a factorized result where single poles in  $n - 4$ , and single logarithms in both cutoffs  $\delta_c$  and  $\delta_s$ , multiply splitting functions and lower-order squared matrix elements. Terms of order  $\delta_c$  and  $\delta_s$  are neglected. The soft and final state hard collinear singularities cancel upon addition of the interference of the leading order diagrams with the renormalized one-loop virtual diagrams. The remaining initial state collinear singularities are factorized and absorbed into the parton distributions. The integrations over the singularity-free portion of the three-body phase space  $H\overline{C}$  are performed using standard Monte Carlo techniques. When all of the contributions are combined at the histogramming stage the cutoff dependences cancel, provided one looks at a suitably defined infrared-safe observable. An example will be given below.

The matrix elements squared for all two-to-two and two-to-three parton-parton scattering subprocesses through  $\mathcal{O}(\alpha_s^3)$  are from the paper of Ellis and Sexton [17], and those for the photon-parton scattering subprocesses through  $\mathcal{O}(\alpha\alpha_s^2)$  are from the paper of Aurenche *et al.* [18].

In order to compare with experimental data, a suitable jet definition must be chosen. For this study, the Snowmass algorithm [19] has been used, supplemented with an  $R_{\text{sep}}$  constraint [20] as follows. Let  $\eta_i$  ( $\eta_j$ ) be the pseudorapidity and  $\phi_i$  ( $\phi_j$ ) be the azimuthal angle of parton  $i$  ( $j$ ) and then define

$$R_{ij} = [(\eta_i - \eta_j)^2 + (\phi_i - \phi_j)^2]^{1/2}. \quad (2.5)$$

Partons  $i$  and  $j$  are merged if

$$R_{ij} \leq \min \left[ \frac{E_{T_i} + E_{T_j}}{\max(E_{T_i}, E_{T_j})} R, R_{\text{sep}} \right]. \quad (2.6)$$

Note that  $R_{\text{sep}} = 2R$  corresponds to having no  $R_{\text{sep}}$  constraint. The 4-vector recombination is of the type

$$\begin{aligned} E_T^{\text{jet}} &= E_T^i + E_T^j \\ \eta^{\text{jet}} &= (\eta^i E_T^i + \eta^j E_T^j) / E_T^{\text{jet}} \\ \phi^{\text{jet}} &= (\phi^i E_T^i + \phi^j E_T^j) / E_T^{\text{jet}}. \end{aligned} \quad (2.7)$$

Other types of jet algorithms may also be used.

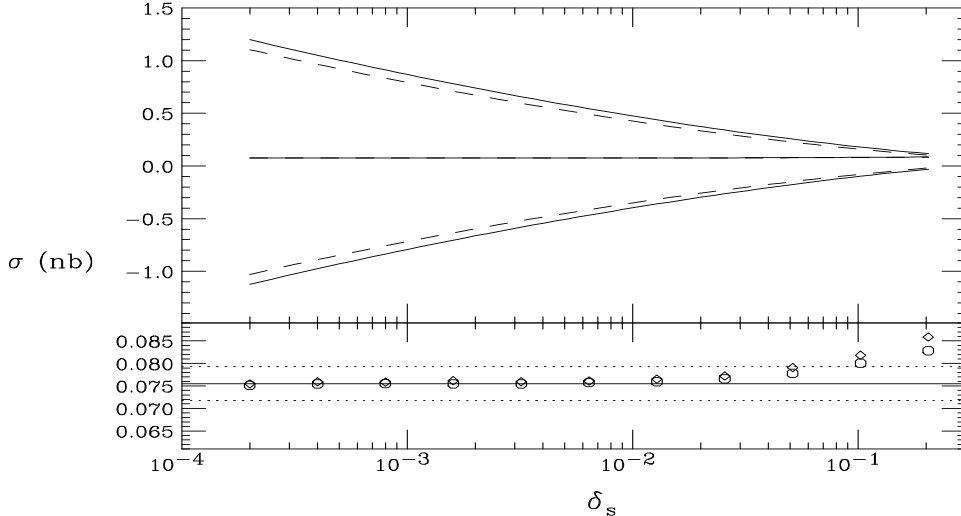


FIG. 1. The single jet inclusive cross section integrated over  $30 \text{ GeV} < E_T^{\text{jet}} < 40 \text{ GeV}$  and  $0 < \eta^{\text{jet}} < 2$ . The two-body (negative) and three-body (positive) contributions together with their sum are shown as a function of  $\delta_s$  with  $\delta_c = \delta_s/a$  for  $a = 100$  (dash line) and  $a = 200$  (solid line). The bottom enlargement shows the sum for  $a = 100$  (circles) and  $a = 200$  (diamonds) relative to  $\pm 5\%$  (dot line) of the average of the last four points (solid line).

### III. RESULTS

#### A. General properties

Using the results of the method described in the previous section we have constructed a program to calculate jet photoproduction cross sections. The program uses Monte Carlo integration so it is possible to implement experimental cuts, provided that they are defined in terms of partonic variables.

The CTEQ4 [21] proton parton distribution set was used throughout, in conjunction with either the GRV [22] or GS [23] photon set. Unless otherwise noted, the GRV set was used. The calculation was performed in the  $\overline{\text{MS}}$  factorization scheme. Therefore, the corresponding  $\overline{\text{MS}}$  distribution sets were used when working at next-to-leading order (NLO). For leading order (LO) results, the appropriate LO sets were used. Similarly, the two-loop version of the strong coupling  $\alpha_s$  was used with matching across quark thresholds for the NLO results, and at LO the one-loop value was used. The value of  $\Lambda^{\text{QCD}}$  was taken from the proton parton distribution set.

For future use we define three sets of beam energy and tagging conditions as follows: 1993 H1 where  $E_e = 26.7 \text{ GeV}$ ,  $E_p = 820 \text{ GeV}$ ,  $Q_{\text{max}}^2 = 0.01 \text{ GeV}^2$  and  $0.25 < y < 0.7$ , 1993 ZEUS where  $E_e = 26.7 \text{ GeV}$ ,  $E_p = 820 \text{ GeV}$ ,  $Q_{\text{max}}^2 = 4 \text{ GeV}^2$  and  $0.2 < y < 0.85$ , and finally 1994 ZEUS where  $E_e = 27.5 \text{ GeV}$ ,  $E_p = 820 \text{ GeV}$ ,  $Q_{\text{max}}^2 = 4 \text{ GeV}^2$  and  $0.25 < y < 0.8$ .

As explained above, when contributions from the two-body and three-body pieces are combined to form a suitably defined infrared-safe observable the cutoff dependences cancel. This provides a check on the method and also on its implementation. As stated in Sec.

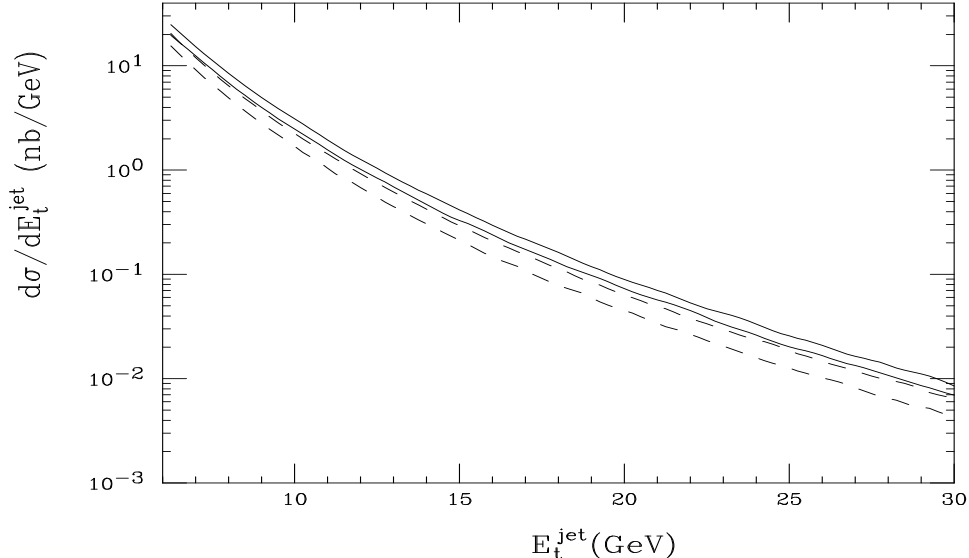


FIG. 2. Scale dependence of the single jet inclusive cross section as a function of  $E_T^{\text{jet}}$  integrated over  $-1 < \eta^{\text{jet}} < 2$ . The LO (dash line) and NLO (solid line) results are shown for two different scale choices,  $\mu = E_T^{\text{max}}/2$  (top) and  $\mu = 2E_T^{\text{max}}$  (bottom).

II, the method requires that  $\delta_c \ll \delta_s$ . Therefore, we take  $\delta_c = \delta_s/a$  with  $a \sim \mathcal{O}(100)$  and verify that the result is independent of  $a$ . As an example, the single jet inclusive cross section integrated over  $30 \text{ GeV} < E_T^{\text{jet}} < 40 \text{ GeV}$  and  $0 < \eta^{\text{jet}} < 2$  is shown in FIG. 1 for the 1994 ZEUS conditions with  $R = 1$  and  $R_{\text{sep}} = 2$ . The two-body (negative) and three-body (positive) contributions together with their sum are shown as a function of  $\delta_s$  for  $a = 100$  (dash line) and  $a = 200$  (solid line). The bottom enlargement shows the sum for  $a = 100$  (circles) and  $a = 200$  (diamonds) relative to  $\pm 5\%$  (dot line) of the actual result (solid line). For this particular observable, the result is sufficiently independent of the cutoffs below  $\delta_s = 10^{-2}$ .

One of the primary reasons for carrying out a NLO calculation is that of reducing factorization and renormalization scale dependence. This is illustrated in FIG. 2 for the single jet inclusive cross section as a function of  $E_T^{\text{jet}}$  integrated over  $-1 < \eta^{\text{jet}} < 2$  for the 1993 H1 conditions with  $R = 1$  and  $R_{\text{sep}} = 2$ . The factorization and renormalization scales have been set equal to  $\mu$ . The LO (dash line) and NLO (solid line) results are shown for two different scale choices  $\mu = E_T^{\text{max}}/2$  (top) and  $\mu = 2E_T^{\text{max}}$  (bottom) where  $E_T^{\text{max}}$  is the maximum transverse energy associated with the relevant two- or three-body weight. The single jet inclusive cross section as a function of  $\eta^{\text{jet}}$  integrated over  $E_T^{\text{jet}} > 15 \text{ GeV}$  is shown in FIG. 3. In both cases, the NLO calculation shows reduced scale dependence relative to the LO result.

As stated in the introduction, it is conventional to describe jet photoproduction in terms of two components. The direct or point-like component corresponds to the case where the photon participates wholly in the hard-scattering subprocess, whereas the resolved or hadron-like component corresponds to a situation where the photon interacts as if it contained partons. In the direct component there is, then, no remnant beam jet and this leads to a simpler event structure than in the purely hadronic case. The decomposition is,

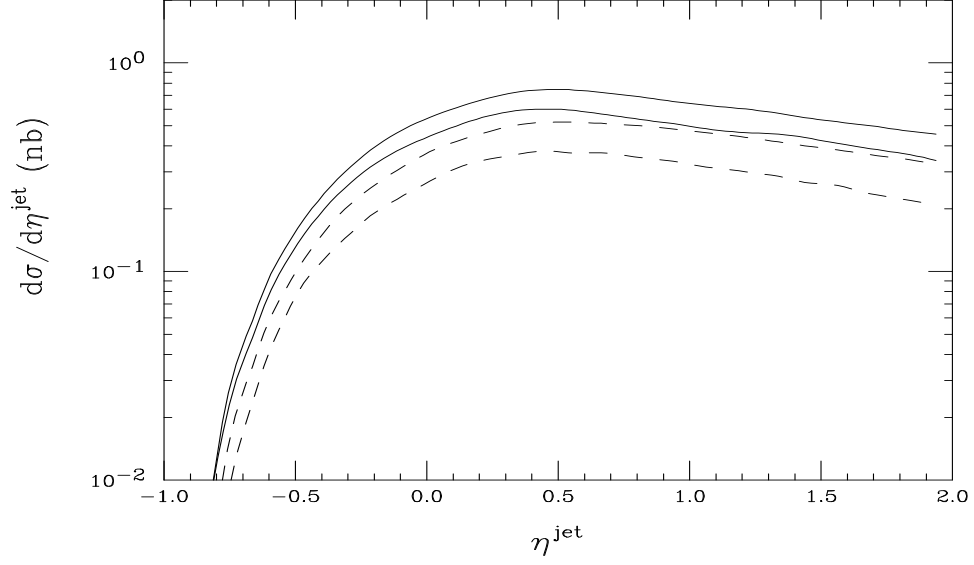


FIG. 3. Scale dependence of the single jet inclusive cross section as a function of  $\eta^{\text{jet}}$  integrated over  $E_T^{\text{jet}} > 15 \text{ GeV}$ . The LO (dash line) and NLO (solid line) results are shown for two different scale choices  $\mu = E_T^{\text{max}}/2$  (top) and  $\mu = 2E_T^{\text{max}}$  (bottom).

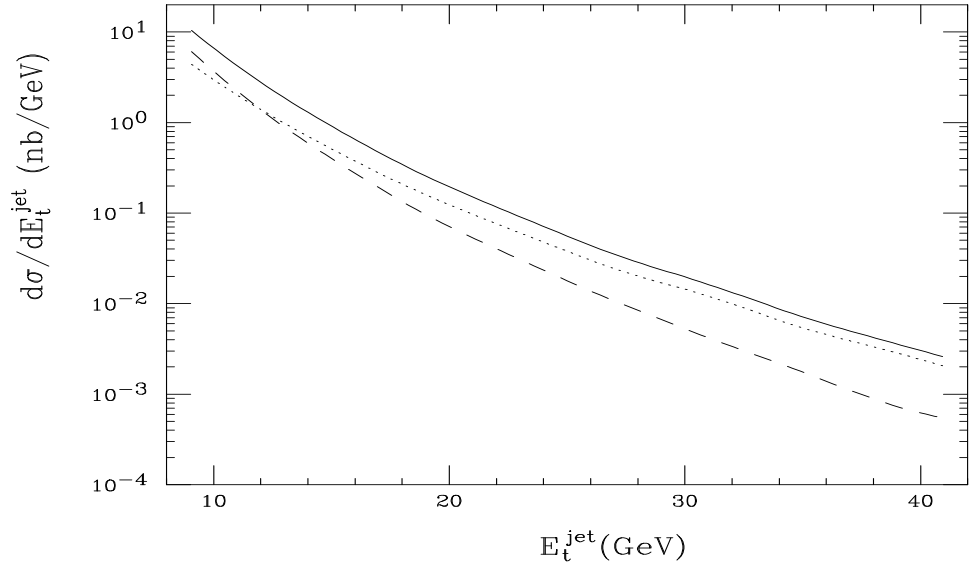


FIG. 4. The NLO single jet inclusive cross section as a function of  $E_T^{\text{jet}}$  integrated over  $-1 < \eta^{\text{jet}} < 2$  in three different regions  $0 < x_\gamma < 1$  (solid),  $x_\gamma > 0.75$  (dot), and  $x_\gamma < 0.75$  (dash).

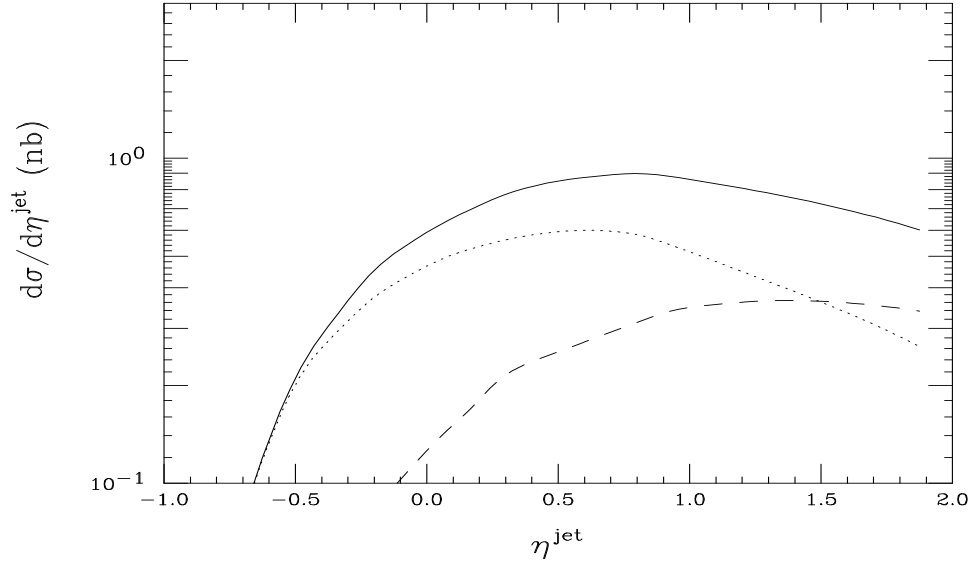


FIG. 5. The NLO single jet inclusive cross section as a function of  $\eta^{\text{jet}}$  integrated over  $E_T^{\text{jet}} > 17$  in three different regions  $0 < x_\gamma < 1$  (solid),  $x_\gamma > 0.75$  (dot), and  $x_\gamma < 0.75$  (dash).

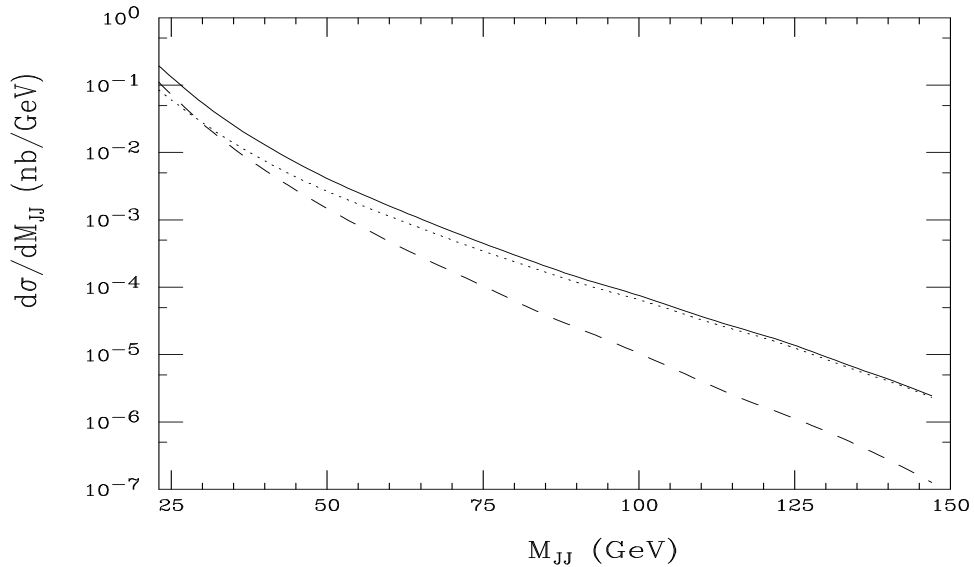


FIG. 6. Dijet cross section as a function of the invariant mass of the two highest  $E_T$  jets decomposed into the regions  $0 < x_\gamma < 1$  (solid),  $x_\gamma > 0.75$  (dot), and  $x_\gamma < 0.75$  (dash).

however, an artifact of viewing the process from the perspective of leading order QCD. At next-to-leading order, the two components mix and a complete separation is not possible.

Although a strict separation into direct and resolved components is not possible, one can still define kinematic regions where either component dominates. One such definition [24] uses the *observed* momentum fraction  $x_\gamma$  of the parton coming from the photon which is given by

$$x_\gamma = (E_T^{\text{jet}1} e^{-\eta_{\text{jet}1}} + E_T^{\text{jet}2} e^{-\eta_{\text{jet}2}}) / 2E_\gamma. \quad (3.1)$$

Here  $E_T$  and  $\eta$  are those of the two highest transverse energy jets. The region  $x_\gamma > 0.75$  corresponds primarily to the direct contribution and  $x_\gamma < 0.75$  to the resolved contribution.

It is interesting to see how the two components populate phase space. To this end, shown in FIG. 4 is the NLO single jet inclusive cross section as a function of  $E_T^{\text{jet}}$  integrated over  $-1 < \eta^{\text{jet}} < 2$  in three different regions  $0 < x_\gamma < 1$  (solid),  $x_\gamma > 0.75$  (dot), and  $x_\gamma < 0.75$  (dash) for the 1993 ZEUS conditions with  $R = 1$ , and  $R_{\text{sep}} = 2$ . The cross section dominated by the resolved component has a steeper  $E_T$  dependence than that which is dominated by the direct component. This is due to the extra convolution associated with the photon parton distribution. In other words, only a portion of the photon's energy contributes to the hard scattering for the resolved component. Hence, at large  $E_T$  values the direct component dominates. In FIG. 5 the NLO single jet inclusive cross section is shown as a function of  $\eta^{\text{jet}}$  integrated over  $E_T^{\text{jet}} > 17$  GeV. The direct component dominates at negative rapidity whereas the resolved component takes over in the positive direction. In the coordinate system used in the HERA experiments, positive rapidity corresponds to the direction of the proton beam. Therefore, if the observed jet is in the positive rapidity region, this corresponds to larger  $x$  values from the proton and smaller ones from the photon. Conversely, if the jet is in the negative rapidity region, larger photon  $x$  values and smaller proton  $x$  values are favored. Since the contribution dominated by the direct component has  $x_\gamma > 0.75$ , it dominates in the negative rapidity region, as shown. In FIG. 6 the dijet cross section is shown as a function of the invariant mass of the two highest  $E_T$  jets. Again, the steeper resolved component dominates over the flatter direct component at low  $M_{\text{JJ}}$ .

## B. Comparison to single inclusive data

Having discussed the general properties of the predictions, it is of interest to see how they compare with existing data. The first comparison is to the single jet inclusive cross sections as measured by H1 [25]. The single jet inclusive cross section as a function of  $E_T^{\text{jet}}$  along with our NLO result (GS photon: solid lines, GRV photon: dash lines) for the 1993 H1 conditions with  $\mu = E_T^{\text{max}}$ ,  $R = 1$ , and  $R_{\text{sep}} = 2$  is shown in FIG. 7. The data and theory have different slopes with the theory falling below the data at low  $E_T^{\text{jet}}$  for both photon sets. The agreement is slightly better for the case where  $\eta^{\text{jet}} < 1$ . This is seen more clearly in FIG. 8 which shows the single jet inclusive cross section as a function of  $\eta^{\text{jet}}$  for  $E_T^{\text{jet}} > E_T^{\text{min}}$  with  $E_T^{\text{min}} = 7, 11, \text{ and } 15$  GeV. In the proton direction the theory consistently undershoots the data. The agreement improves as  $E_T^{\text{min}}$  increases. One possible explanation for the observed discrepancy may be the need to increase the gluonic content of the photon which is poorly constrained in this  $x$  region. However, this would be premature as underlying event

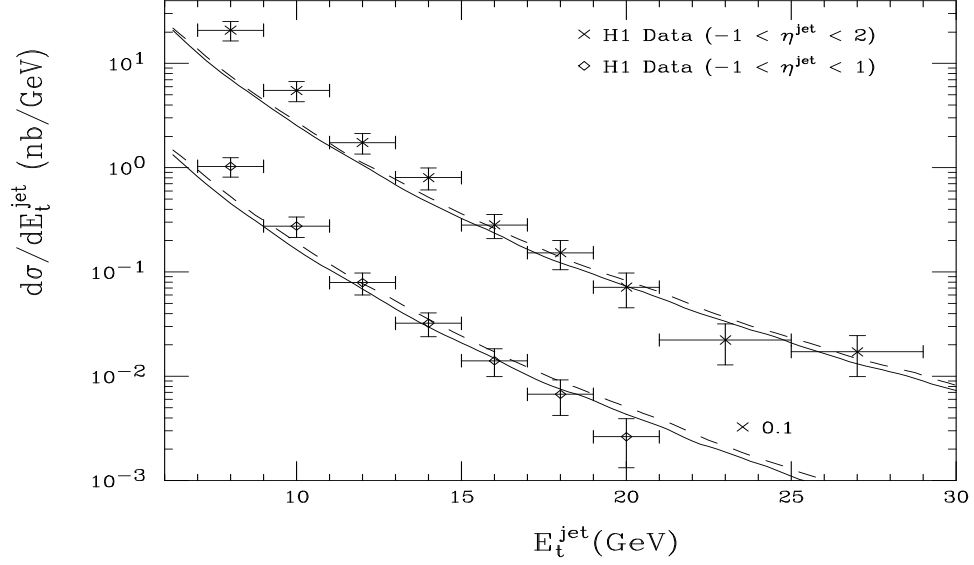


FIG. 7. The single jet inclusive cross section as a function of  $E_T^{\text{jet}}$  as measured by H1 [25] compared with our NLO result (GS photon: solid lines, GRV photon: dash lines).

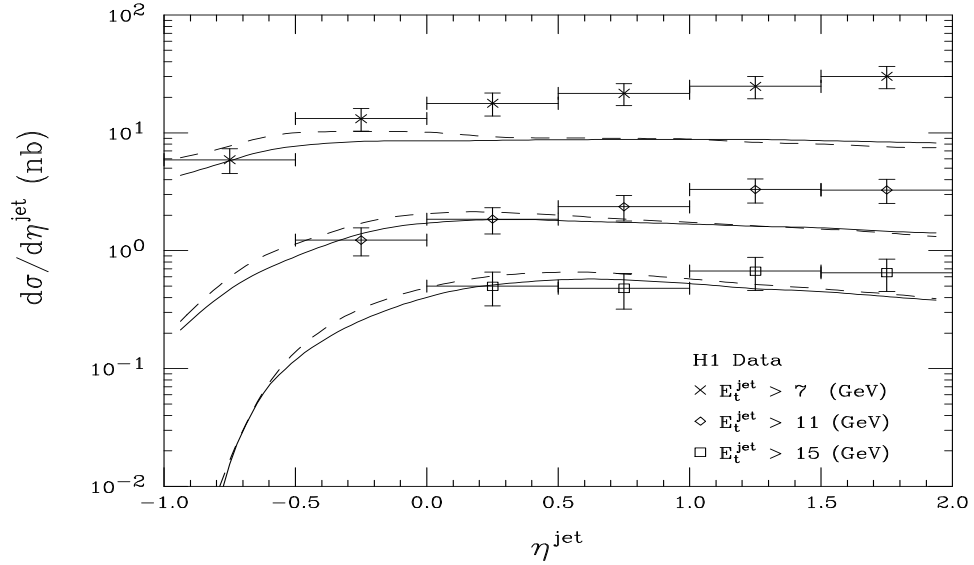


FIG. 8. The single jet inclusive cross section as a function of  $\eta^{\text{jet}}$  as measured by H1 [25] compared with our NLO result (GS photon: solid lines, GRV photon: dash lines).

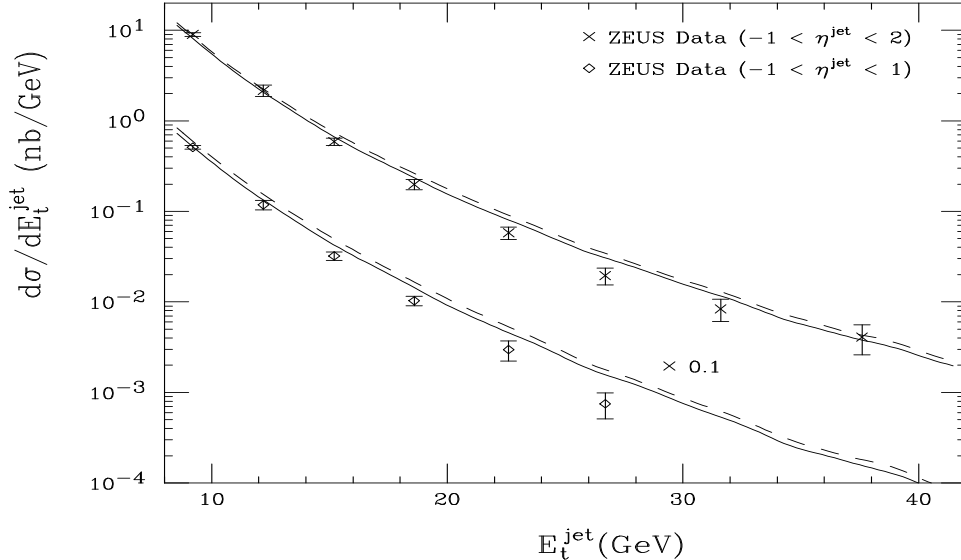


FIG. 9. The single jet inclusive cross section as a function of  $E_T^{\text{jet}}$  as measured by ZEUS [26] compared with our NLO result (GS photon: solid lines, GRV photon: dash lines).

contributions, which were not removed from the data set or included in our calculation, may also provide an explanation.

We next switch to 1993 ZEUS conditions and compare to the published ZEUS data [26] on single jet inclusive cross sections. In FIG. 9 the measured single jet inclusive cross section is shown as a function of  $E_T^{\text{jet}}$  along with our NLO result (GS photon: solid lines, GRV photon: dash lines) with  $\mu = E_T^{\text{max}}$ ,  $R = 1$ , and  $R_{\text{sep}} = 2$ . In this case the agreement with the data is somewhat better than that shown in FIG. 7. This is further illustrated by the comparison with the single jet inclusive cross section as a function of  $\eta^{\text{jet}}$ , shown in FIG. 10. The trend, although less pronounced, is the same as with the H1 data.

### C. Comparison to dijet data

Data for several different types of observables involving two large transverse momentum jets have been published. In the ZEUS dijet analysis a sample of dijet events is obtained by requiring  $E_T^{\text{jet}_1}, E_T^{\text{jet}_2} > E_T^{\text{min}}$ . In principle, this presents a problem in the following sense. The pair of jets can be accompanied by additional soft gluons. The singularities associated with the soft gluon emission cancel infrared singularities coming from one-loop contributions. This cancellation has already taken place in the present calculation. That is, the soft gluons with energies up to  $\delta_s \sqrt{s_{12}}/2$  have already been integrated out. After the cancellation there are residual  $\ln \delta_s$  terms in the two-body portion of the calculation which cancel against logarithms built up by integrating over the unobserved gluon radiation in the three body contribution. The requirement that both jets have  $E_T > E_T^{\text{min}}$  restricts a portion of this integration and leads to an incomplete cancellation of the  $\ln \delta_s$  dependence. We have, nevertheless, used this definition for the dijet sample, having found that the cutoff dependence of the results is negligible. However, the problem still exists, at least in principle.

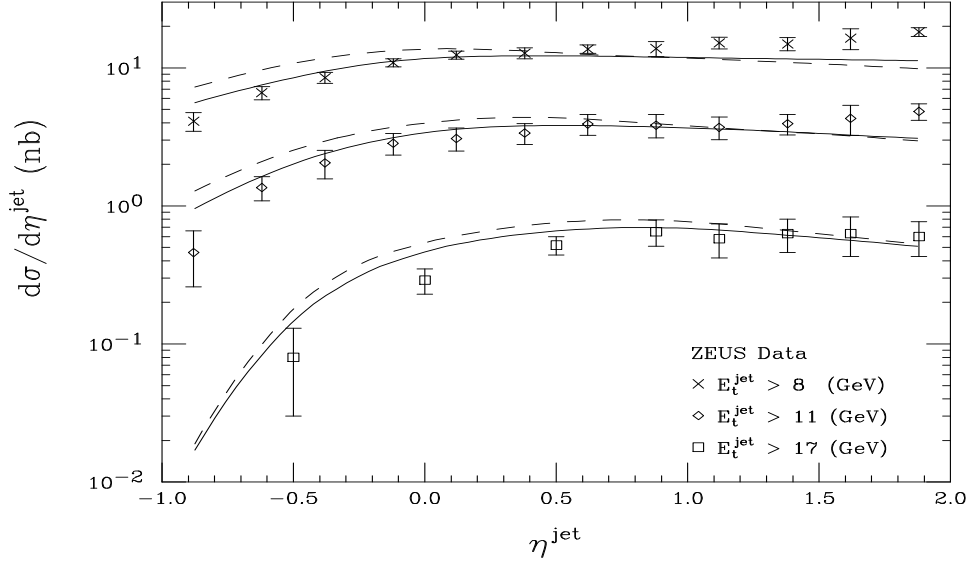


FIG. 10. The single jet inclusive cross section as a function of  $\eta^{\text{jet}}$  as measured by ZEUS [26] compared with our NLO result (GS photon: solid lines, GRV photon: dash lines).

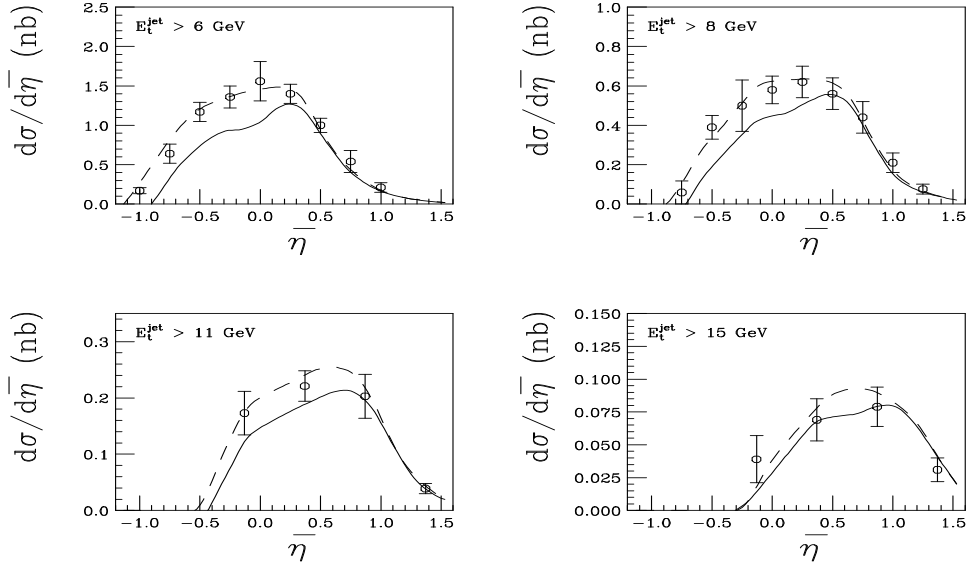


FIG. 11. Dijet cross section for  $x_\gamma > 0.75$  as a function of  $\bar{\eta}$  integrated over  $E_T^{\text{jet}} > E_T^{\text{min}}$  for  $E_T^{\text{min}} = 6, 8, 11, 15$  GeV as measured by ZEUS [27]. The solid curves correspond to requiring  $E_T^{\text{jet}1}, E_T^{\text{jet}2} > E_T^{\text{min}}$  while the dashed curves correspond to the cuts used in [12], as described in text.

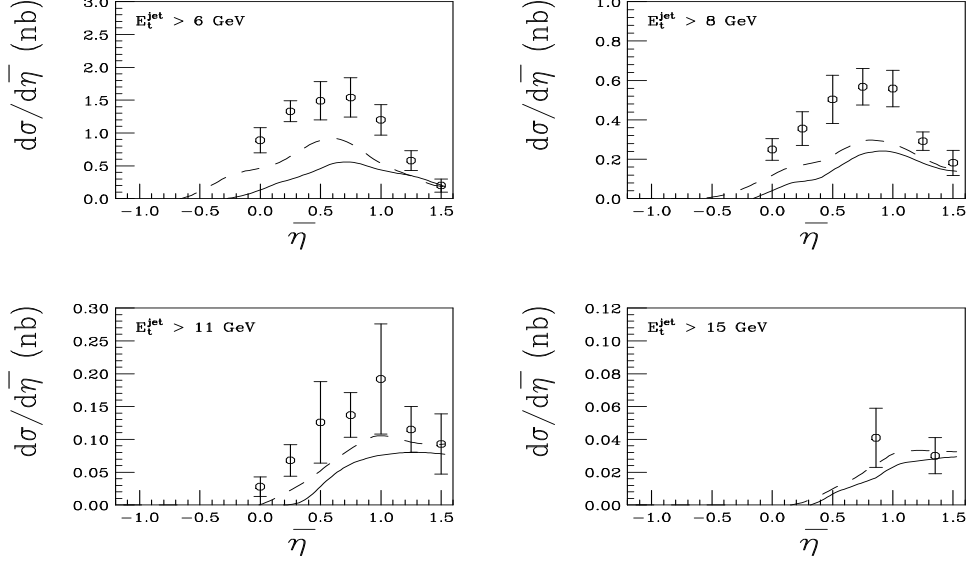


FIG. 12. Dijet cross section for  $0.3 < x_\gamma < 0.75$  as a function of  $\bar{\eta}$  integrated over  $E_T^{\text{jet}} > E_T^{\text{min}}$  for  $E_T^{\text{min}} = 6, 8, 11, 15$  GeV as measured by ZEUS [27]. The solid curves correspond to requiring  $E_T^{\text{jet}_1}, E_T^{\text{jet}_2} > E_T^{\text{min}}$  while the dashed curves correspond to the cuts used in [12], as described in text.

Preliminary ZEUS data [27] for the dijet cross section as a function of  $\bar{\eta} = (\eta^{\text{jet}_1} + \eta^{\text{jet}_2})/2$  integrated over  $|\eta^{\text{jet}_1} - \eta^{\text{jet}_2}| < 0.5$  are shown in FIGS. 11 and 12 for  $E_T^{\text{jet}_1}, E_T^{\text{jet}_2} > E_T^{\text{min}}$  with  $E_T^{\text{min}} = 6, 8, 11, \text{ and } 15$  GeV. The solid curves are our results for the 1994 ZEUS conditions using the GRV photon set,  $\mu = E_T^{\text{max}}$ , and  $R = 1$ . A value of  $R_{\text{sep}} = 1$  was used following [28] where it was found that this value used at the parton level most closely corresponds to the KTCLUS algorithm used to define the jets. No systematic cutoff dependence was observed for these results, within the limitations of the Monte Carlo errors. The solid curves display the same trend that was observed in the single inclusive plots discussed previously insofar as the direct component comes closer to the data than does the resolved, the data are underestimated in the low  $E_T$  region, and the agreement gets better as  $E_T^{\text{min}}$  increases. This is consistent with there being some residual underlying event contribution to the observed jets which has not been removed during the data analysis.

The problem of defining a sample of two jet events in a manner which is amenable to a next-to-leading order theoretical treatment has been studied in [12]. In order to avoid a dependence on the theoretical cutoffs used in the course of the calculation, it was proposed to calculate the dijet cross section by allowing the second jet to have a transverse energy less than  $E_T^{\text{min}}$  if the third unobserved jet is soft, i.e. has a transverse energy of less than 1 GeV ( $E_T^{\text{jet}_3} < 1$  GeV). This approach slightly expands the available phase space when both jets have transverse energies near  $E_T^{\text{min}}$  and, therefore, avoids the problem of a potential cutoff dependence. Results using this algorithm are shown in FIGS. 11 and 12 by the dashed lines. The relaxation of the  $E_T^{\text{min}}$  constraint on the second jet generates additional contributions from the  $2 \rightarrow 3$  subprocesses so that the dashed curves lie above the solid ones and are in better agreement with the data. However, the cuts do not correspond to those utilized in the definition of the data sample. Given the unresolved question of the underlying event

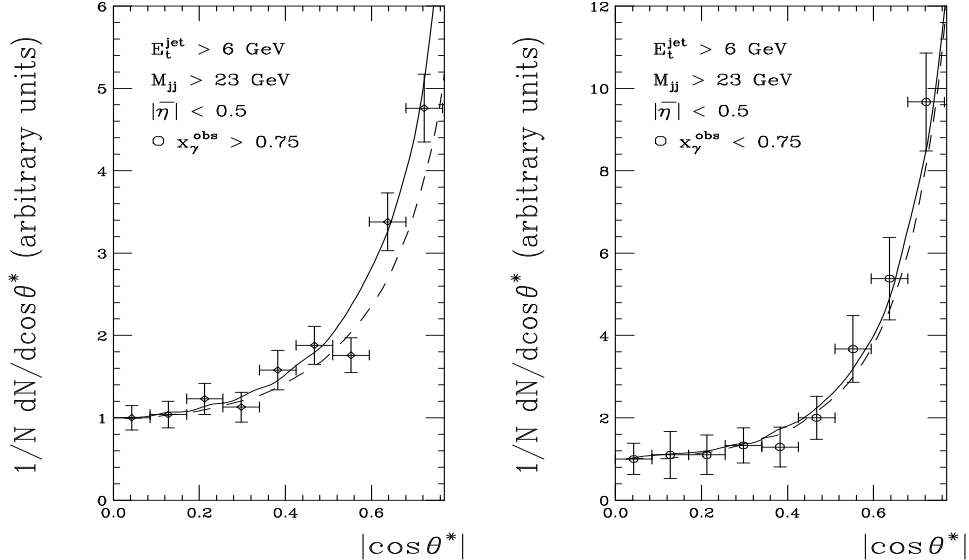


FIG. 13. Dijet angular distribution  $d\sigma/d|\cos\theta^*|$  as measured by ZEUS [29] normalized to one at  $\cos\theta^* = 0$  compared with LO (dash lines) and NLO result (solid lines).

contributions, it is premature to draw detailed conclusions from comparisons with these data.

Angular distributions in dijet production are sensitive to the spin of the exchanged particle. Let  $\theta^*$  be the scattering angle of the two highest  $E_T$  jets in their center of mass. In LO, the direct component is dominated by  $t$ -channel quark exchange which has a characteristic angular dependence given by  $(1 - |\cos\theta^*|)^{-1}$ . The resolved component, however, is dominated by  $t$ -channel gluon exchange and has a  $(1 - |\cos\theta^*|)^{-2}$  angular dependence. This property is preserved at NLO as demonstrated by the solid lines in FIG. 13 where the dijet angular distribution  $d\sigma/d|\cos\theta^*|$  is shown as a function of  $|\cos\theta^*|$  in the regions  $x_\gamma > 0.75$  (left) and  $x_\gamma < 0.75$  (right) for the 1994 ZEUS conditions with  $R = 1$ , and  $R_{\text{sep}} = 2$ . Also shown in the figure is the ZEUS [29] measurement and the LO (dash line) result. To better compare shapes, the distributions are normalized to one at  $|\cos\theta^*| = 0$ . The shapes are very insensitive to how one handles the dijet definition issue discussed above. The excellent agreement between the predictions and the data confirms the theoretically expected behavior.

#### IV. CONCLUSION

In this paper, results from a new next-to-leading-order program for jet photoproduction have been presented. The calculation was performed using the phase space slicing method and implemented in a Monte Carlo style program. Physical observables are independent of the phase space slicing parameters.

As is the case in other jet production processes, the renormalization and factorization scale dependence is reduced relative to leading-order predictions. A decomposition into direct and resolved components was also studied using a definition based on the observed

momentum fraction of the parton from the photon. The direct component dominates at large  $E_T$  and in the photon direction while the resolved dominates at low  $E_T$  and in the proton direction.

Comparisons with single inclusive jet cross section measurements by H1 and ZEUS as a function of  $E_T^{\text{jet}}$  and  $\eta^{\text{jet}}$  show that the theory tends to lie somewhat below the data in the forward rapidity region. This is the region corresponding to low values for  $x_\gamma$  and which is dominated by the resolved component. One might suspect that this indicates a need for increasing the size of the photon parton distributions in this  $x$  range, but this conclusion would be premature since contributions from underlying event structure could account for this, as well.

Our results were also compared with dijet cross section measurements from ZEUS. The cuts used to define the dijet sample are such as to restrict a portion of the phase space needed to insure the proper cancellation of the cutoff dependence in the two- and three-body contributions. In practice, however, the variation was found to be smaller than the statistical errors associated with the Monte Carlo integrations. This point aside, the predictions for the normalized angular distributions agree well with the data. The  $\bar{\eta}$  distributions show the same pattern of deviations from the theoretical predictions as was observed in the single inclusive jet measurements.

As additional data are acquired it is possible that jet photoproduction will be used to place additional constraints on the parton distributions in the photon. Such data would complement data for the photon structure function which are primarily sensitive to the quark distributions in the photon. The jet photoproduction process, on the other hand, directly involves the gluon distribution in the photon. However, in order for such data to provide useful constraints on the photon parton distributions, the effects of the underlying event structure must be minimized. Higher  $E_T$  thresholds combined with a smaller cone size in the jet definition would help in this regard.

## REFERENCES

- [1] J.F. Owens, *Phys. Rev. D* **21**, 54 (1980).
- [2] M. Drees and R. Godbole, *J. Phys. G* **21**, 1559 (1995).
- [3] H. Baer, J. Ohnemus and J.F. Owens, *Phys. Rev. D* **40**, 2844 (1989).
- [4] D. Bödeker, *Phys. Lett. B* **292**, 164 (1992); *Z. Phys. C* **59**, 501 (1993).
- [5] M. Klasen and G. Kramer, *Z. Phys. C* **72**, 107 (1996).
- [6] L.E. Gordon and J.K. Storrow, *Phys. Lett. B* **291**, 320 (1992).
- [7] M. Greco and A. Vicini, *Nucl. Phys. B* **415**, 386 (1994).
- [8] P. Aurenche, J.-Ph. Guillet, and M. Fontannaz, *Phys. Lett. B* **338**, 98 (1994). The results for the resolved component in this paper are overestimated by a factor of two, see [13].
- [9] G. Kramer, and S.G. Salesch, *Z. Phys. C* **61**, 277 (1994); D. Bödeker, G. Kramer, and S.G. Salesch, *Z. Phys. C* **63**, 471 (1994); M. Klasen, G. Kramer, and S.G. Salesch, *Z. Phys. C* **68**, 113 (1995).
- [10] G. Kramer, *J. Phys. G* **22**, 717 (1996).
- [11] B.W. Harris and J.F. Owens, in Proceedings of American Physical Society, Division of Particles and Fields 1996 Meeting (to be published).
- [12] M. Klasen and G. Kramer, DESY 96-246.
- [13] P. Aurenche, L. Bourhis, M. Fontannaz, and J.-Ph. Guillet, in *Proceedings of the Workshop 1995/96 on Future Physics at HERA, Hamburg, 1996*, edited by G. Ingelman *et al.* (Deutsches Elektronen-Synchrotron, Hamburg, 1996), p. 570.
- [14] L.J. Bergmann, Ph.D. thesis, Florida State University, 1989.
- [15] C.F. Weizsäcker, *Z. Phys.* **88**, 612 (1934); E.J. Williams, *Phys. Rev.* **45**, 729 (1934).
- [16] S. Frixione, M.L. Mangano, P. Nason and G. Ridolfi, *Phys. Lett. B* **319**, 339 (1993).
- [17] R.K. Ellis and J.C. Sexton, *Nucl. Phys. B* **269**, 445 (1986).
- [18] P. Aurenche, R. Baier, A. Douiri, M. Fontannaz, and D. Schiff, *Nucl. Phys. B* **286**, 553 (1987). The expressions for the  $qq \rightarrow qq\gamma$  and  $qq' \rightarrow qq'\gamma$  subprocesses contain a number of typographical errors where the variable  $a_3$  appears in place of  $a_5$ . The original report LPTHE Orsay 86/24 contains the correct expressions.
- [19] J. Huth *et al.*, *Proc. of the 1990 DPF Summer Study on High Energy Physics, Snowmass, Colorado*, edited by E.L. Berger (World Scientific, Singapore, 1992) p. 134.
- [20] S.D. Ellis, Z. Kunszt and D.E. Soper, *Phys. Rev. D* **40**, 2188 (1989).
- [21] H.L. Lai *et al.*, *Phys. Rev. D* **55**, 1280 (1997).
- [22] M. Glück, E. Reya and A. Vogt, *Phys. Rev. D* **46**, 1973 (1992).
- [23] L.E. Gordon and J.K. Storrow, *Nucl. Phys. B* **489**, 405 (1997).
- [24] ZEUS Collab. (M. Derrick *et al.*), *Phys. Lett. B* **348**, 665 (1995).
- [25] H1 Collab. (S. Aid *et al.*), *Z. Phys. C* **70**, 17 (1996).
- [26] ZEUS Collab. (M. Derrick *et al.*), *Phys. Lett. B* **342**, 417 (1995).
- [27] ZEUS Collab. (M. Derrick *et al.*), talk pa02-040, presented at the XXVIII International Conference on High Energy Physics, Warsaw, Poland, July 25-31, 1996.
- [28] J.M. Butterworth, L. Feld, M. Klasen, and G. Kramer, in *Proceedings of the Workshop 1995/96 on Future Physics at HERA, Hamburg, 1996*, edited by G. Ingelman *et al.* (Deutsches Elektronen-Synchrotron, Hamburg, 1996), p. 554.
- [29] ZEUS Collab. (M. Derrick *et al.*), *Phys. Lett. B* **384**, 401 (1996).